Ultrarobust Thin-Film Devices from Self-Assembled Metal–Terpyridine Oligomers

Zoi Karipidou, Barbara Branchi, Mustafa Sarpasan, Nikolaus Knorr, Vadim Rodin, Pascal Friederich, Tobias Neumann, Velimir Meded, Silvia Rosselli, Gabriele Nelles, Wolfgang Wenzel, Maria Anita Rampi, and Florian von Wrochem**

The promise of integrating functional organic molecules into nanoscale junctions, enabling feature-size reduction and the control of electrical properties by molecular design has been the driving force in nanoelectronics over the past decades.[1,2] Although organic molecules have been characterized in a number of experimental test-beds,[3] the realization of robust and practical molecular devices remained a challenge. Specifically, a major hurdle toward the practical realization of solid state molecular junctions turned out to be the deposition of metal electrodes because the conventional process (e.g., physical vapor deposition or sputtering) generally leads to damage/electrical shorts experienced by the fragile molecular layers.[4,5] The problem becomes insurmountable when moving to large area junctions spanning several thousands of μm^2.[6] Thus, a number of sophisticated approaches emerged[3] to mitigate electrical shorting and to provide a platform suited for the electrical characterization of small molecular ensembles (e.g., conductive atomic force microscopy (AFM),[7,8] nanopore junctions[9] or dense molecular layers (e.g., Hg-drop[10–12] and eutectic GaIn[13] junctions). In spite of the considerable mechanistic understanding gained with these techniques, the integration of organic layers into solid state junctions remains a challenge. For this reason, the development of alternative electrode deposition methods with the potential for device integration was brought forward, such as indirect evaporation[14] or lift-off float on deposition.[15,16] More recently, polymeric,[6] graphene,[17] or inorganic[13,18] interlayers have been introduced to protect ultrathin molecular layers from invasive, vapor deposited contacts. These approaches represent a promising pathway toward robust molecular/polymer circuits; however they require an additional organic/inorganic layer that inevitably masks the intrinsic electrical response of the molecules under investigation. A possible solution has been proposed by McCreery and co-workers, involving molecular layers that are sandwiched between carbon and copper electrodes forming stable and highly reproducible molecular junctions.[19] Remarkably, these large area junctions show high yields, endurance, and temperature stability, even though the requirement of using pyrolytic carbon as a bottom electrode might limit their applicability.

Here, we demonstrate that by integration of Fe^{II}–terpyridine redox complex oligomers[20–22] into large area solid-state junctions, molecular thin-film devices of outstanding mechanical and electrical robustness are realized. Notwithstanding the metallic crossbar junctions are deposited in a conventional thermal evaporation process, Fe^{II}–terpyridine oligomers are operational over a period of more than two and a half years and resist to temperatures ranging from 150–360 K. The oligomer layers show a high electron mobility (μ_e = 0.1 $cm^2\ V^{-1}\ s^{-1}$) and, most remarkably, electrical transport follows an ideal Richardson–Schottky (RS) injection behavior, as demonstrated by means of complementary experimental and theoretical investigations.

Bottom electrodes are prepared by thermal evaporation of an array of eight parallel Au electrodes (each 100 µm wide) on native silicon using a shadow mask. Subsequently, metal center oligomers (MCOs) are deposited by a stepwise sequential coordination reaction of a Fe^{II} redox center by a conjugated 1,4-di(2;2′;6′;2″-terpyridine-4′-yl)benzene (TPT) ligand (**Figure 1**a),[21] as schematically depicted in Figure 1b. In our work, oligomers of three different lengths have been assembled by incorporation of 15, 20, and 30 Fe^{II} metal centers (MC), yielding MCO layers with a thickness of 15, 20, and 30 nm. This allows a detailed study of their electrical characteristics as a function of molecular length. A symmetric contact of the oligomers to both Au electrodes is established by using 4′-(4-mercaptophenyl)terpyridine (MPTP) as the first and last ligands of the stepwise coordination.

From density functional theory (DFT) calculations, a length of 1.55 nm is derived for the repeat unit of the MCO chain (Figure 1a). A constant increment in film thickness as a function of the coordination number is determined from AFM data (Figure 1c), following a linear regression with a slope of ≈1.08 nm per coordination step. These data and the coordination efficiency known for the stepwise coordination process[23]

Z. Karipidou, M. Sarpasan, Dr. N. Knorr, Dr. V. Rodin, Dr. S. Rosselli, Dr. G. Nelles, Dr. F. von Wrochem
Sony Deutschland GmbH
Materials Science Laboratory
Hedelfinger Strasse 61, 70327 Stuttgart, Germany
E-mail: Florian.vonWrochem@eu.sony.com

Dr. B. Branchi, Prof. M. A. Rampi
Dipartimento di Chimica
Università di Ferrara
Via Borsari 46, 44100 Ferrara, Italy
E-mail: rmp@unife.it

P. Friederich, T. Neumann, Dr. V. Meded, Prof. W. Wenzel
Institute of Nanotechnology
Karlsruhe Institute of Technology
76021 Karlsruhe, Germany

DOI: 10.1002/adma.201504847

ADVANCED MATERIALS
www.advmat.de

www.MaterialsViews.com

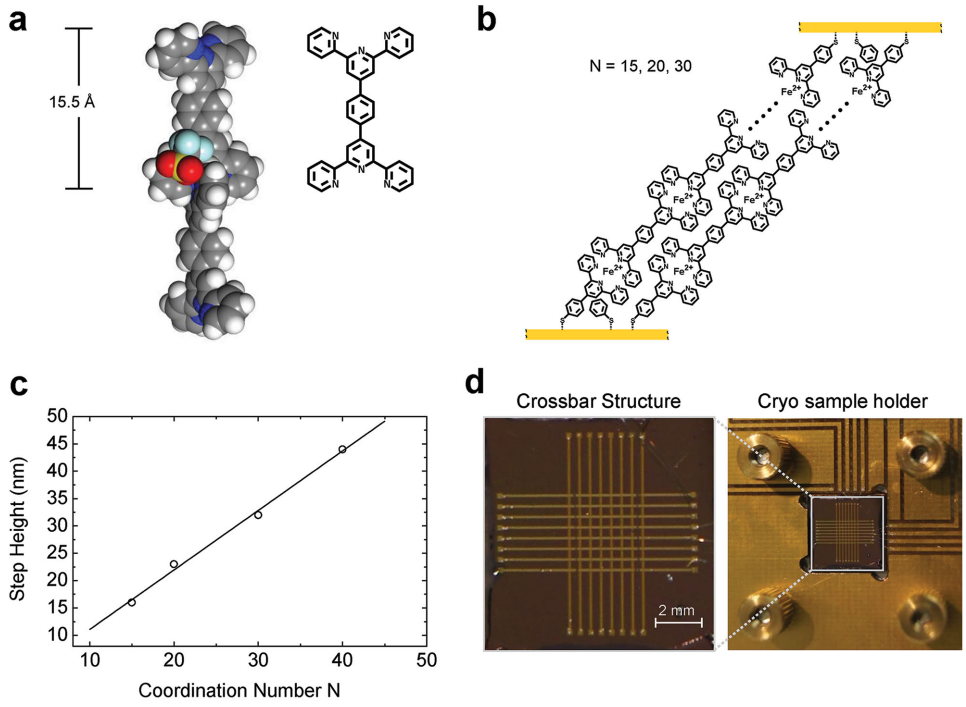

Figure 1. Schematic representation of the metal–terpyridine-based oligomers and of the crossbar device structures. a) Molecular structure of the TPT ligand and energy minimized geometry of a TPT dimer from DFT calculations. b) Scheme of an array of MCO oligomers bridging two Au contacts. For clarity, the triflate counter-ions are not included in the scheme; they are however part of the theoretical model presented in Figure 5 c) Dependence of the step height on the number of MC deposition cycles from AFM measurements. A linear fit to the data results in an increase of the MCO layer thickness by 1.08 nm per coordination number. The data point with 40 MCs serves to verify the linearity of the film deposition. d) Picture of the Au/MCO/Au crossbar structure before characterization in a cryostat.

supports a well-defined self-limiting layer-by-layer build-up.[24] Based on the repeat unit length and the thickness extracted from AFM data, the MCO oligomer assumes a tilt angle of ≈46° from the surface normal. The chemical structure of the layers is confirmed by X-ray photoemission spectroscopy.

The microstructure of the films is investigated by molecular simulations using molecule-specific all-atom force-fields obtained from density functional calculations on preoptimized molecular building blocks (see Figure 5 and the Supporting Information for details). The simulations of the MCOs (including the triflate counter-ions) indicate that a maximum in lateral packing density and energetic stability is reached at a tilt angle of 46.6°, very close to the value obtained from AFM measurements. Bulky Fe^{II}–terpyridine moieties interlock with the less bulky aromatic "bridges" of the neighboring oligomers to form a structure with calculated density of 0.96 g cm^{-3}. The counter-ions compensate the Coulomb repulsion between the positive oligomer-based Fe^{II}-ions. We calculated the average distance between the counter-ions and the nearest Fe^{II}-ion to be 6.4 ± 0.5 Å. The fairly narrow distribution throughout the sample indicates strong electrostatic interaction and, thus, the major role of counter-ions in the stacking of the oligomers.

In contrast to previous work on metal-complex multilayer films,[25] which reported the use of PEDOT:PSS as a protective interlayer against invasive top metal electrodes, herein the electrodes are deposited directly on the MCO layer by thermal evaporation (55 nm of Au at a deposition rate of 0.02 nm s^{-1}) using the same electrode pattern as employed for the bottom electrodes, however rotated by 90°.[26] The resulting devices (Figure 1d) consist of 64 junctions with an area of 100 µm × 100 µm at each cross point. The samples are stored under nitrogen atmosphere, and extensive electrical characterization is carried out under high vacuum (HV) conditions (base pressure: 10^{-6} mbar) using a cryostat and an automated data acquisition system. **Figure 2**a shows the *J*–*V* curves, acquired using a bias interval of 50 mV and 120 µs per data point (see the Supporting Information for details on measurements and statistics). Junctions incorporating 15, 20, and 30 MCs were capable of sustaining bias voltages ranging from −3 V to 3 V, corresponding to a maximum electric field of ≈2×10^6 V cm^{-1}. Our data shows a remarkable reproducibility from junction to junction, as well as for hundreds of sequential *J*–*V* scans from the same junction. The majority of the devices showed no degradation during our study. In Figure 2d the first and the last measurement within a durability tests is shown, demonstrating the outstanding long-term stability of MCO junctions over a lifetime of two and a half years. The functional shape of the *J*–*V* traces is roughly preserved, demonstrating that the conclusions from RS analysis are consistent over the time of our study.

The stability of the junctions is remarkable considering the invasiveness of vapor-deposited gold electrodes that commonly induce shorts in molecular layers, which can only be avoided by the use of additional polymer[6] or graphene[17] interlayers. We experimentally elucidate the mechanical stability of the films in nanowear experiments using Silicon AFM probes with loads between 100 nN and 2 µN (Figure S4, Supporting Information).

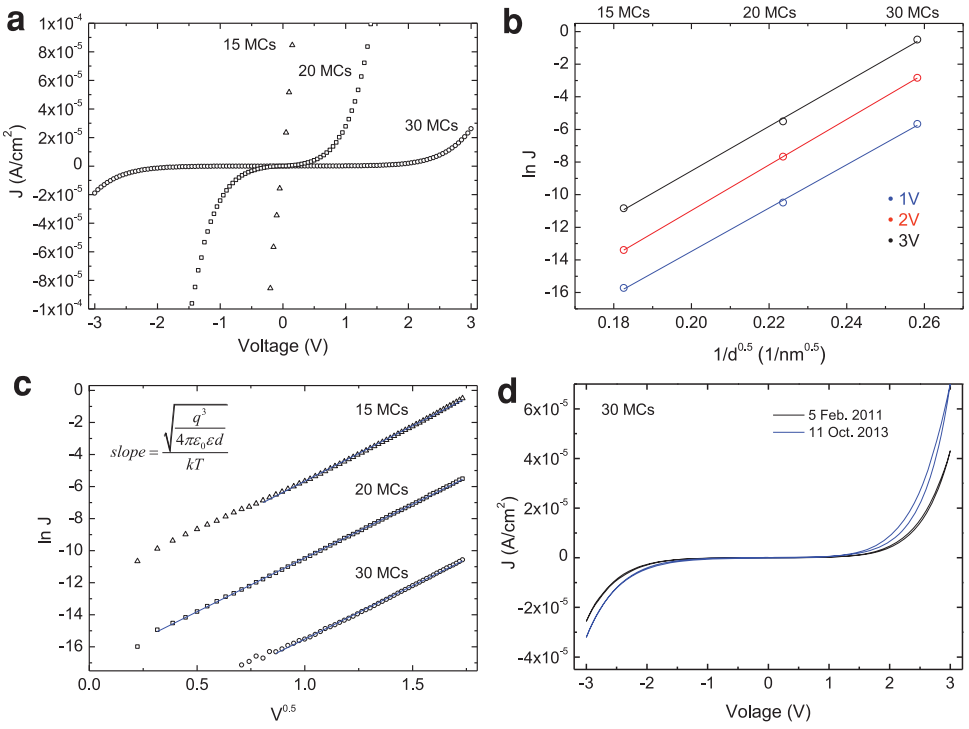

Figure 2. Electrical data from Au/MCO/Au junctions, incorporating 15, 20, and 30 MCOs measured at room temperature (pressure: 10^{-6} mbar). a) *J–V* characteristics. b) Semi-log plot of the current density ln(*J*) versus $1/d^{0.5}$, following a linear regression as expected from Equation (1). c) RS plot showing the linear dependence of ln(*J*) on $V^{0.5}$. The data in (a), (b), and (c) represent the average from *J–V* measurements on several samples. d) Durability test of MCO junctions, showing the lifetime of the junction with 30 MCs over a time of two and a half years (see the Supporting Information for details on statistics and lifetime).

MCO films thereby show an even higher wear robustness than PMMA layers, which is attributed to a strong intermolecular stabilization (electrostatic intermolecular attraction and π–π interactions), a dense packing, and the additional chemical bond to the substrate. Note that the junctions are temperature stable from 150 to 360 K, which allows the extraction of key parameters such as charge-injection barrier, dielectric constant, Richardson constant, and mobility (vide infra).

Nonresonant tunneling is the commonly accepted mechanism for charge transport through ultrathin molecular monolayers.[10,27,28] In a few cases, temperature-dependent hopping transport was observed.[29,30] Recently, it has been demonstrated that the transition from tunneling to a hopping regime occurs at a critical molecular length of ≈3–4 nm.[31,32] Thus, we assume that for Au/MCO/Au junctions the hopping regime is applicable.

To investigate charge transport in Au/MCO/Au junctions, we examine the dependence of the *J–V* characteristics on voltage, film thickness, and temperature, and fit these data to different theoretical models. In Figure 2a, the *J–V* curves for Au/MCO/Au junctions with 15, 20, and 30 MCs are shown. Neither a nonresonant tunneling model[27] predicting an exponential decay behavior according to $J = J_0 e^{-\beta d}$ (where β is the decay constant and d the distance) nor space charge limited transport (the Mott–Gurney law)[33] could fit our data (Figure S5 and S6, Supporting Information). The only appropriate Ansatz appears to be injection-limited transport, known to prevail for high injection barriers between the Fermi level of the contact and the transport levels of the semiconductor. Thermionic emission,[34,35] an injection process based on thermal activation, is known to be effective in systems exhibiting hopping transport, such as polymers[36] or amorphous molecular layers commonly used in organic light-emitting diodes (OLEDs).[37] This regime is rarely reported in molecular thin-film devices,[38] essentially because its observation requires molecular building blocks that are: i) long enough for charge transport being not exclusively governed by tunneling,[9,31] and ii) stable enough to withstand a sufficient range of temperatures and bias voltages. For our analysis, we apply a model recently introduced by Scott and Malliaras,[39] where in the strong field limit (>10^5 V cm^{-1}) the expression for the current density reduces to the well-known RS Ansatz for thermionic emission:[40,41]

$$J = A^{*}T^{2} e^{(-\phi_b/kT)} e^{\left(\sqrt{q^3 V/4\pi\varepsilon_0\varepsilon d}/kT\right)} \quad (1)$$

with A^* being the effective Richardson constant, ϕ_b the energy barrier for hole/electron injection (Schottky barrier), ε the dielectric constant, ε_0 the permittivity of vacuum, k the Boltzmann constant, and q the electronic charge.

Figure 2b shows a plot of ln(*J*) versus the inverse square root of the layer thickness *d*. The linear fit demonstrates the excellent agreement of the measured currents with the RS model according to Equation (1), providing first evidence for thermionic emission in MCO junctions. This interpretation is substantiated by an analysis of the *J–V* dependence, as shown in the plot of ln(*J*) versus $V^{1/2}$ (Figure 2c). As expected for RS emission, we observe linear

behavior in compliance with Equation (1), the slope representing the RS coefficient (slope = $d(\ln J)/d(\sqrt{V})$, see inset in Figure 2c). Remarkably, the RS model applies to Au/MCO/Au junctions with MCO oligomers of different length, with currents spanning five decades (at 3 V). Small deviations from linearity as observed in Figure 2c for short MCOs (15 MCs) are attributed to residual moisture present in the molecular layers (as observed before in bis(terpyridine)Fe^{II} crystals).[42] As a matter of fact, the removal of traces of H_2O from the MCO layer, either by storage under HV conditions for several days or by thermal annealing, appears to be crucial to obtain well defined *J*–*V* characteristics (see the Experimental Section for details). Under these conditions, our *J*–*V* data show ideal Schottky emission behavior (Figure S7, Supporting Information), which is a nontrivial result considering the ionic nature of the organic layer under investigation, and the possibility of drift currents from impurities and water.[10]

Understanding charge transport in molecular scale devices, specifically in view of thermally activated processes, requires the electrical characterization over a wide temperature range. This was possible thanks to the extraordinary structural stability of MCO junctions, which allowed *J*–*V* measurements with *T* from 150 to 360 K, thus enabling the extraction of key material parameters such as the dielectric constant ε, the charge-injection barrier ϕ_b, and the effective Richardson constant *A**. **Figure 3**a illustrates the dependence of the RS coefficient (slope of ln(*J*) vs $V^{1/2}$) and the intercept J_0 (linear fit at 0 V) on the temperature for MCO junctions with 20 MCs. From the slope of the RS coefficient versus $1/T$ (Figure 3b), the dielectric constant is obtained ($\varepsilon = 2.43$), and found to be in good agreement with independent ellipsometric measurements ($\varepsilon = 2.73$, vide infra). Equation (1), in the zero bias limit, reduces to $\ln(J_0) = \ln(A^2T^2) - \phi_b/kT$, providing the parameter *A** for known values of the intercept J_0. As shown in the inset of Figure 3b, *A** is found to be temperature independent in the range from 250 to 360 K, a further evidence for the applicability of the RS model (Equation (1)). By using $\phi_b = 0.72$ eV (vide infra), we find that $A^* = 0.5$ A cm^{-2} K^{-2}, which is much closer to the Richardson constant for free electrons ($A^* = 4\pi q m^* k^2/h^3 = 120$ A cm^{-2} K^{-2}) than experimental values reported for disordered hopping systems such as OLED materials ($A^* \approx 10^{-8}$ A cm^{-2} K^{-2}).[37] For comparison, typical values of *A** for inorganic semiconductors range from 1.7 to 258 A cm^{-2} K^{-2}.[43] Applying the Scott–Malliaras model[39] in the strong field limit ($F \approx 10^6$ V cm^{-1}), the Richardson constant reduces to $A^* \approx 6\pi\varepsilon\varepsilon_0 N_0 \mu k^2/e_2$, where N_0 is the density of hopping sites and μ is the mobility in the organic film (see the Transport Models section in the Supporting Information). With this, we estimate the mobility in MCO layers as $\mu \approx 0.1$ cm^2 V^{-1} s^{-1}, a surprisingly high value that we attribute to the structural order of the Fe^{II}–terpyridine oligomers in π-conjugated MCO layers, as well as to the overlap of π* orbitals of neighboring TPT units (vide infra). It compares favorably with disordered organic small molecule semiconductors ($\approx 10^{-4}$ cm^2 V^{-1} s^{-1}) and polymers such as regioregular P3HT (0.1 cm^2 V^{-1} s^{-1}).[44]

Figure 3c shows a plot of $\ln(J/T^2)$ versus $1/T$, from which the injection barrier ϕ_b is extracted by using Equation (2)

$$\ln\left[\frac{J}{T^2}\right] = \ln A^* + \left(\left(-\phi_b + \sqrt{\frac{q^3V}{4\pi\varepsilon_0\varepsilon d}}\right)\frac{1}{k}\right)\frac{1}{T} \quad (2)$$

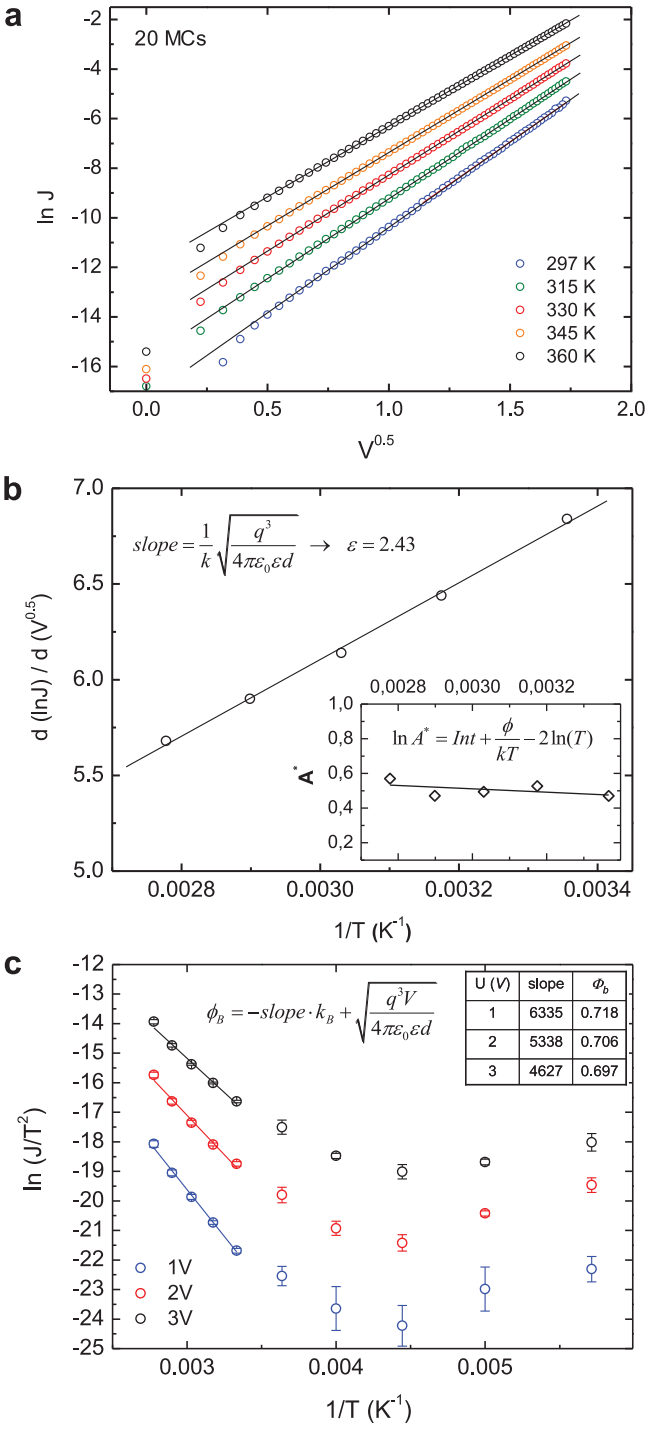

Figure 3. Temperature-dependent *J*–*V* data. a) RS plot of the current density as a function of temperature for Au/MCO/Au junctions with 20 MCs. From the slope of the linear fits as well as from the temperature and the film thickness, the average static dielectric constant ε is derived (see equation in (b)). b) RS coefficient versus $1/T$ as obtained from the slopes shown in (a), yielding a dielectric constant of $\varepsilon = 2.43$. The intercept of the linear fits at $V = 0$ (see graph in (a)) gives the parameter *A**. In the inset of (b), the dependence of *A** on $1/T$ is shown. c) $\ln(J/T^2)$ versus $1/T$ plot for MCO junctions with 20 MCs ($d = 20$ nm). From the linear fit to the data above 250 K, the charge-injection barrier is derived at bias voltages of 1, 2, and 3 V. Slopes and calculated injection barriers are shown in the inset. Values are mean ± SEM.

The plot is acquired at three different bias voltages (1, 2, and 3 V) and shows a temperature-dependent linear regime above 250 K and a nearly temperature independent regime below 250 K, which is reminiscent of the behavior observed in carbon/self-assembled monolayer (SAM)/copper junctions.[19] The Schottky barrier ϕ_b (i.e. the energy gap between the metal Fermi level and the highest occupied molecular orbital (HOMO) or lowest unoccupied molecular orbital (LUMO) of the organic material) is obtained from the high-temperature asymptote, i.e., from a linear fit to the data in the regime above 250 K, resulting in an injection barrier of $\phi_b \approx 0.72$ eV (Figure 3c, inset table).[40] We conclude that charge injection in Au/MCO/Au junctions is governed by the Schottky barriers at the contacts, which in turn are defined by the chemistry of the aromatic TPT ligands representing the hopping sites for electron transport (vide infra).

Notably, Fowler–Nordheim (FN) tunneling is excluded as a possible injection mechanism. In fact, currents in the FN regime are inherently temperature independent (whereas our data is not, see Figure 3c),[40] and would result in a linear slope in the FN plots (Figure S8, Supporting Information). We estimate that significantly higher electrical fields are necessary to reach FN tunneling for MCO junctions.

To provide a sound basis for our interpretation in terms of RS emission, we have extracted a number of material parameters from independent optical, electrochemical, and spectroscopic investigations, and used them to validate our model. By ellipsometric measurements, a dielectric constant of $\varepsilon = 2.73 \pm 0.2$ is obtained for MCO layers with 30 MCs (Supporting Information), which is in excellent agreement with values extracted from electrical data ($\varepsilon = 2.43$). The injection barrier ϕ_b depends on the position of the energy levels of the HOMO and LUMO of the organic material with respect to the Fermi level of the metal electrodes. The levels have been determined by cyclic voltammetry (CV) measurements in solution using the model compound $Fe^{II}(ttpy)_2$ that is structurally analogue to the MCO complexes, as well as with a thin MCO film consisting of 4 MCs deposited onto the Au working electrode (see **Figure 4**a and Figure S9, S14, and S15, Supporting Information). Based on the oxidation and reduction potentials, the HOMO and LUMO levels are found to be at 5.8 and 3.5 eV, respectively. Low-intensity XPS spectra (LI-XPS; Figure 4b) yield a work function of 4.29 eV for MCO-coated Au electrodes (15 MCs), compared to 5.1 eV for clean, argon-sputtered Au substrates. This work-function shift results from the push-back effect[45] and the interface dipole created by the thiolate layer,[46] both known to reduce the work function of Au by about 1 eV.[26,47] Combining the data from LI-XPS and CV, an energy diagram as shown in Figure 4c is derived, where the downshift of the HOMO and LUMO levels of MCO by 1.0 eV relative to the Fermi level of polycrystalline Au (reported to have a work function of 5.3 eV),[48] has been included. Notably, the injection barrier between the Fermi level of Au and the LUMO of MCO

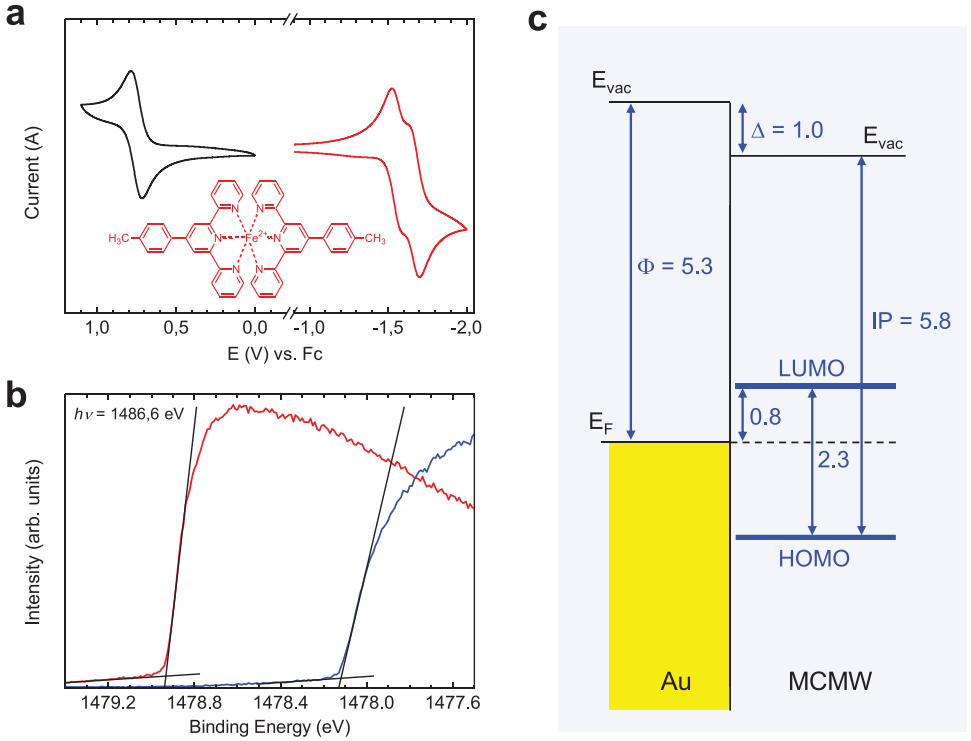

Figure 4. Extraction of the energy level diagram from electrochemical and spectroscopic data. a) Cyclic voltammograms showing the Fe^{II}–Fe^{III} redox process of the model compound $Fe^{II}(ttpy)_2$ in acetonitrile solution (0.8×10^{-3} M, $TBAPF_6$ 0.1 M), with oxidation (black) and reduction (red) peaks at $E_{1/2}^{ox} = 0.67$ and $E_{1/2}^{red} = -1.64$ V (vs Fc/Fc^+), respectively. b) Secondary cutoff of an Ar-sputtered Au substrate (blue) and of an MCO-modified Au surface (red) with 15 MCs as obtained from LI-XPS data. The measured work function is 5.1 and 4.29 eV, respectively. c) Energy diagram (at zero bias) of the Au/MCO interface resulting from CV and LI-XPS data, where a work function of 5.3 eV is assumed for a polycrystalline Au surface.[48] Note that the formation of a pronounced depletion zone in the organic layer (at the contact), as known for doped semiconductors, is excluded as it would induce an interface dipole with a related work function offset that is not observed here.

is reduced to ϕ_b = 0.8 eV upon molecular assembly, which is in excellent agreement with the Schottky barrier as determined from electrical measurements (0.72 eV).

Based on the consolidated experimental data, we conclude that charge transport in Au/MCO/Au junctions takes place by electron conduction. A substantial ballistic contribution to the electronic transport would require a strong electronic overlap matrix element between directly adjacent moieties along the molecule. The π-character of the LUMOs (shown in **Figure 5**c,d, generates nonzero hopping matrix elements between adjacent linkers only if they are not perpendicular, which corresponds to the symmetric conformation with respect to the Fe-center. For this reason, we first examine the stiffness of the angle between adjacent linkers that complexate the Fe^{II} redox center. The energy profile for the rotation of the terpyridine group around the molecular axis (Figure S10, Supporting Information) indicates that the intermoiety angle is confined to nearly 90°, and as a consequence, the direct hopping matrix element of adjacent π orbitals is small (indeed $J_{direct} = 4.19 \times 10^{-3}$ eV; see Table S1, Supporting Information). In combination with the large unit cell this leads to extremely flat bands. We also find that the reorganization energy (≈0.2 eV; see the Supporting Information) is considerably larger than the direct hopping matrix element, which indicates that the charge hopping is much slower than charge relaxation processes. Both observations point to a loss of coherence of mobile carriers, i.e., the absence of band transport. For this reason, we investigate electron transport both along the MCO oligomer (on-wire) and between adjacent oligomers (off-wire) (Figure 5a) within the context of a hopping transport model, i.e., by analyzing the hopping matrix elements of all relevant processes. Figure 5c presents the LUMO and LUMO+1 along a "Cardan-joint" of the oligomer. Some of the possible on-wire and off-wire hopping sites are indicated in Figure 5d along with the corresponding LUMOs. The distribution of coupling matrix elements[49] (Table S1, Supporting Information) clearly demonstrates that the on-wire and the largest off-wire hopping matrix elements have comparable magnitudes. Consequently, hopping transport on-wire and off-wire are equally

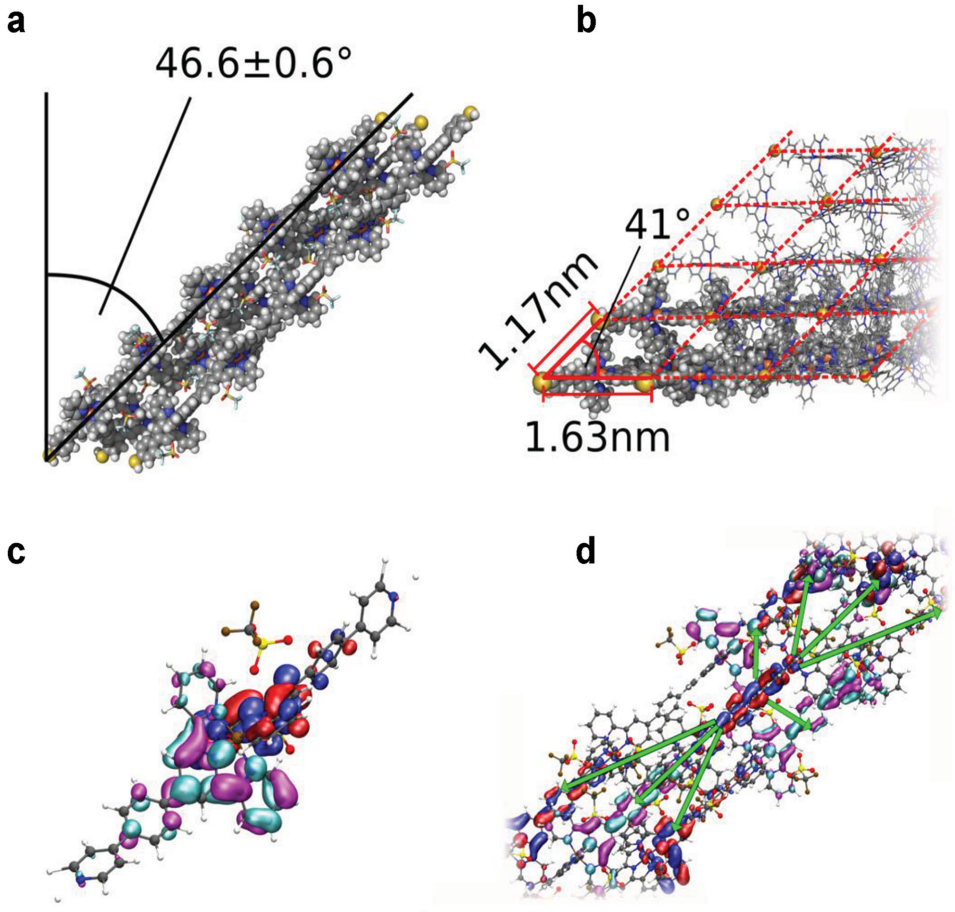

Figure 5. Microscopic and electronic structure of MCO layers. a) Side view of the optimized structure of the MCO trimer (counter-ions explicitly included) with the oligomer center-of-mass fixed in the *z*-direction (counter-ions were not restricted). After a full relaxation in the *xy*-plane, the lowest energy structure resulted in an angle of 46.6° between the surface normal and the molecular backbone. b) Top view of the same MCO trimer, with lattice parameters a = 16.3 Å, b = 11.7 Å, and an angle of 41° between a and b. The structure is periodically extendable as illustrated by continuation of the MCO oligomers in the *xy*-plane (in "stick" representation). c) LUMO (red and blue) and LUMO+1 (cyan and pink) orbital along the oligomer, in the "Cardan-joint" part of the MCO structure. The LUMO orbitals have predominant π, out of plane character. The estimated hopping matrix element between the indicated orbitals is 2.44×10^{-3} eV. d) The LUMO orbitals, in alternating colors (see (c)) along the MCO trimer. Green lines illustrate hopping sites away from a chosen central site.

likely, which is consistent with the robustness of experimental transport measurements. We estimate the electron mobility using a recently developed analytic approach,[50] obtaining $\mu_e = 0.22 \times 10^{-1}$ cm^2 V^{-1} s^{-1}, which is not far from the value that results from experimental data with the Scott–Malliaras model ($\mu_e = 10^{-1}$ cm^2 V^{-1} s^{-1}). The expectedly much lower estimate of the hole mobility, $\mu_h = 3.1 \times 10^{-4}$ cm^2 V^{-1} s^{-1}, is a consequence of much stronger localization of HOMO states, that are dominated by Fe^{II} *d*-electron states.

Both by experiment and theory, we have shown that metal-center terpyridine oligomers form highly cohesive molecular assemblies, producing ultrathin films of remarkable mechanical robustness and electrical stability. The film properties enable the fabrication of robust large area junctions by conventional thermal deposition of the top metal electrodes, so being compliant with standard manufacturing processes. The temperature stability of the junctions allows for detailed electrical studies, and in conjunction with ab initio calculations, we reveal that charge transport: i) occurs via electron (hopping) conduction both along and off the wire, and ii) is limited by the charge injection through a Schottky barrier with $\phi_b = 0.72$ eV following a prototypical Richardson–Schottky model. The outstanding lifetime and stability makes these junctions candidates for the development of active and passive components in organic electrical circuits. By adjusting the energy levels along the MCO chain (e.g., the LUMO by substitution of the aromatic core) the Schottky barriers at the contacts might be removed, and by tailoring the sequence of the monomers along the MCO chain (including different organic ligands and/or chromophores) device characteristics such as rectification, negative differential resistance, and photoinduced switching might be realized. Still, structural changes in the backbone might affect the packing density of the MCOs; therefore, particular care has to be taken when implementing any new functionality, so to keep their extraordinary mechanical robustness unaltered.

Experimental Section

Preparation: Electrodes were realized by evaporation of 50 nm Au on 5 nm Cr on a Si wafer with 400 nm thermal oxide (sample dimensions: 10 mm × 10 mm). The vapor-deposited gold electrodes were functionalized with an SAM of MPTP/MB (MPTP = 4′-(4-mercaptophenyl)terpyridine, MB = mercaptobenzene), prepared by immersing the electrodes in an equimolar solution of MPTP and MB (5×10^{-5} M each, chloroform, 1 d) and rinsing with chloroform. This provided a stable anchoring of the MCO oligomer to the bottom electrode. The functionalized electrodes were: i) immersed in a solution of $Fe(CF_3SO_3)_2$ (5×10^{-5} M, ethanol:chloroform 1:1, 5 min) and rinsed with ethanol and chloroform, ii) immersed in a TPT solution (TPT = 1,4-di(2;2′;6′;2″-terpyridine-4′-yl)benzene, 5×10^{-4} M, chloroform, 20 min) and rinsed with chloroform and ethanol. Stages (i) and (ii) were repeated iteratively, whereby the Fe^{II} charges were balanced by triflate counter-ions. Once the desired length was reached, the samples were immersed in an MPTP solution (5×10^{-4} M, chloroform, 20 min) providing a thiolate end group and a symmetric layer structure within the molecular junction. By using 15, 20, and 30 iterations, MCO chains having a length of 23.2, 31, and 46.5 nm, respectively, were formed with an overall layer thickness of 15, 20, and 30 nm. The top electrodes were defined by vapor deposition of 55 nm of Au using a shadow mask as stated above, however, rotated by 90° (see Figure 1d).

Electrical Measurements: Currents were measured under HV conditions (base pressure: 10^{-6} mbar) using a modified optical cryostat (Oxford Optistat CF-V) and a custom-built automated data acquisition system. As the samples appeared to be quite moisture-sensitive (a pronounced hysteresis in the *I–V* characteristics was found for measurements under ambient conditions), the chips were kept under HV for several days before electrical characterization (ideally for several weeks for hysteresis-free *I–V* curves). For each cross point, 35 *I–V* curves were recorded in the voltage range ±0.5, ±1, ±2, and ±3 V, where each *I–V* trace was acquired using a bias interval of 50 mV and a time of 120 ms per voltage step, corresponding to a scan rate of 0.42 V s^{-1}. In total, ten cross points were measured on each fabricated sample or chip (having 15, 20, or 30 coordination steps, respectively), resulting in 350 traces per sample. The data presented in Figure 2 and 3 resulted from the average of at least 50–60 single *I–V* curves from at least two different chips. As after storage under HV the *I–V* curves showed almost no hysteresis, the forward and reverse sweeps were averaged. For data analysis, traces from shorted junctions were discarded. The samples measured after two and a half years (as shown in Figure 2d) were stored under Argon and measured after a few hours in HV (10^{-6} mbar).

Further experimental details on sample preparation, electrical measurements, ellipsometry, photoemission spectroscopy, cyclic voltammetry, atomic force microscopy, and nanowear measurements are provided in the Supporting Information.

Supporting Information

Supporting Information is available from the Wiley Online Library or from the author.

Acknowledgements

The authors acknowledge A. Roberts for his support in ellipsometry measurements. The authors further wish to thank H.-J. Queisser, H. Bässler, H. Riel, W. E. Ford, and S. Caramori for useful discussion. W.W. acknowledges funding from the Deutsche Forschungsgemeinschaft (WE 1863/21-1) and the program Science and Technology of Nanosystems (STN) at KIT. F.v.W. and W.W. acknowledge financial support from the EU FP7 Project MMM@HPC (No. 261549).

Received: October 1, 2015
Revised: December 10, 2015
Published online: March 10, 2016

[1] A. Aviram, M. A. Ratner, *Chem. Phys. Lett.* **1974**, *29*, 277.
[2] R. L. Carroll, C. B. Gorman, *Angew. Chem. Int. Ed.* **2002**, *41*, 4379.
[3] H. B. Akkerman, B. de Boer, *J. Phys.: Condens. Matter* **2008**, *20*, 013001.
[4] T. W. Kim, G. N. Wang, H. Lee, T. Lee, *Nanotechnology* **2007**, *18*, 315204.
[5] H. Haick, J. Ghabboun, D. Cahen, *Appl. Phys. Lett.* **2005**, *86*, 042113.
[6] H. B. Akkerman, P. W. M. Blom, D. M. de Leeuw, B. de Boer, *Nature* **2006**, *441*, 69.
[7] D. J. Wold, C. D. Frisbie, *J. Am. Chem. Soc.* **2000**, *122*, 2970.
[8] X. D. Cui, A. Primak, X. Zarate, J. Tomfohr, O. F. Sankey, A. L. Moore, T. A. Moore, D. Gust, D. J. Harrison, S. M. Lindsay, *Science* **2001**, *294*, 571.
[9] W. Wang, T. Lee, M. A. Reed, *Phys. Rev. B* **2003**, *68*, 035416.
[10] B. Mann, H. Kuhn, *J. Appl. Phys.* **1971**, *42*, 4398.
[11] R. E. Holmlin, R. Haag, M. L. Chabinyc, R. F. Ismagilov, A. E. Cohen, A. Terfort, M. A. Rampi, G. M. Whitesides, *J. Am. Chem. Soc.* **2001**, *123*, 5075.

[12] F. von Wrochem, D. Gao, F. Scholz, H. G. Nothofer, G. Nelles, J. M. Wessels, *Nat. Nanotechnol.* **2010**, *5*, 618.
[13] R. C. Chiechi, E. A. Weiss, M. D. Dickey, G. M. Whitesides, *Angew. Chem. Int. Ed.* **2008**, *47*, 142.
[14] H. Haick, M. Ambrico, J. Ghabboun, T. Ligonzo, D. Cahen, *Phys. Chem. Chem. Phys.* **2004**, *6*, 4538.
[15] A. Vilan, D. Cahen, *Adv. Funct. Mater.* **2002**, *12*, 795.
[16] K. T. Shimizu, J. D. Fabbri, J. J. Jelincic, N. A. Melosh, *Adv. Mater.* **2006**, *18*, 1499.
[17] T. Li, J. R. Hauptmann, Z. Wei, S. Petersen, N. Bovet, T. Vosch, J. Nygard, W. Hu, Y. Liu, T. Bjornholm, K. Nygaard, B. W. Laursen, *Adv. Mater.* **2012**, *24*, 1333.
[18] M. J. Preiner, N. A. Melosh, *Appl. Phys. Lett.* **2008**, *92*, 213301.
[19] A. J. Bergren, K. D. Harris, F. J. Deng, R. L. McCreery, *J. Phys.: Condens. Matter* **2008**, *20*, 374117–374127.
[20] A. Winter, S. Hoeppener, G. R. Newkome, U. S. Schubert, *Adv. Mater.* **2011**, *23*, 3484.
[21] N. Tuccitto, V. Ferri, M. Cavazzini, S. Quici, G. Zhavnerko, A. Licciardello, M. A. Rampi, *Nat. Mater.* **2009**, *8*, 41.
[22] C. Musumeci, G. Zappalá, N. Martsinovich, E. Orgiu, S. Schuster, S. Quici, M. Zharnikov, A. Troisi, A. Licciardello, P. Samori, *Adv. Mater.* **2014**, *26*, 1688.
[23] N. Tuccitto, V. Torrisi, M. Cavazzini, T. Morotti, F. Puntoriero, S. Quici, S. Campagna, A. Licciardello, *ChemPhysChem* **2007**, *8*, 227.
[24] R. Sakamoto, S. Katagiri, H. Maeda, H. Nishihara, *Coord. Chem. Rev.* **2013**, *257*, 1493.
[25] K. I. Terada, H. Nakamura, K. Kanaizuka, M. A. Haga, Y. Asai, T. Ishida, *ACS Nano* **2012**, *6*, 1988.
[26] W. E. Ford, D. Gao, N. Knorr, R. Wirtz, F. Scholz, Z. Karipidou, K. Ogasawara, S. Rosselli, V. Rodin, G. Nelles, F. von Wrochem, *ACS Nano* **2014**, *8*, 9173.
[27] G. Gamow, *Z. Phys.* **1928**, *51*, 204.
[28] W. Wang, T. Lee, M. A. Reed, *J. Phys. Chem. B* **2004**, *108*, 18398.
[29] Y. Selzer, M. A. Cabassi, T. S. Mayer, D. L. Allara, *J. Am. Chem. Soc.* **2004**, *126*, 4052.
[30] X. Li, J. Hihath, F. Chen, T. Masuda, L. Zang, N. Tao, *J. Am. Chem. Soc.* **2007**, *129*, 11535.
[31] S. H. Choi, B. Kim, C. D. Frisbie, *Science* **2008**, *320*, 1482.
[32] S. H. Choi, C. Risko, M. C. R. Delgado, B. Kim, J. L. Bredas, C. D. Frisbie, *J. Am. Chem. Soc.* **2010**, *132*, 4358.
[33] M. A. Lampert, P. Mark, *Current Injection in Solids*, Academic, New York **1970**.
[34] O. W. Richardson, *Thermionic Phenomena and the Laws Which Govern Them*, Elsevier, Amsterdam, The Netherlands **1965**, p. 1928.
[35] C. Weißmantel, C. Hamann, *Grundlagen der Festkörperphysik*, VEB Deutscher Verlag der Wissenschaften, Berlin, Germany **1981**.
[36] Z. Chiguvare, J. Parisi, V. Dyakonov, *J. Appl. Phys.* **2003**, *94*, 2440.
[37] S. Barth, U. Wolf, H. Bässler, P. Muller, H. Riel, H. Vestweber, P. F. Seidler, W. Riess, *Phys. Rev. B* **1999**, *60*, 8791.
[38] C. Zhou, M. R. Deshpande, M. A. Reed, L. Jonesll, J. M. Tour, *Appl. Phys. Lett.* **1997**, *71*, 611.
[39] J. C. Scott, G. G. Malliaras, *Chem. Phys. Lett.* **1999**, *299*, 115.
[40] S. M. Sze, *Physics of Semiconductor Devices*, Wiley, New York **2012**.
[41] R. R. Das, P. Bhattacharya, W. Perez, R. S. Katiyar, A. S. Bhalla, *Appl. Phys. Lett.* **2002**, *81*, 880.
[42] A. T. Baker, H. A. Goodwin, *Aust. J. Chem.* **1985**, *38*, 207.
[43] W. Mönch, *Electronic Properties of Semiconductor Interfaces*, Springer, Berlin/Heidelberg, Germany, **2004**.
[44] K. M. Coakley, B. S. Srinivasan, J. M. Ziebarth, C. Goh, Y. Liu, M. D. McGehee, *Adv. Funct. Mater.* **2005**, *15*, 1927.
[45] S. Braun, W. R. Salaneck, M. Fahlman, *Adv. Mater.* **2009**, *21*, 1450.
[46] I. H. Campbell, S. Rubin, T. A. Zawodzinski, J. D. Kress, R. L. Martin, D. L. Smith, N. N. Barashkov, J. P. Ferraris, *Phys. Rev. B* **1996**, *54*, 14321.
[47] D. M. Alloway, M. Hofmann, D. L. Smith, N. E. Gruhn, A. L. Graham, R. Colorado, V. H. Wysocki, T. R. Lee, P. A. Lee, N. R. Armstrong, *J. Phys. Chem. B* **2003**, *107*, 11690.
[48] J. E. Lyon, A. J. Cascio, M. M. Beerbom, R. Schlaf, Y. Zhu, S. A. Jenekhe, *Appl. Phys. Lett.* **2006**, *88*, 222109.
[49] P. Friederich, F. Symalla, V. Meded, T. Neumann, W. Wenzel, *J. Chem. Theory Comput.* **2014**, *10*, 3720.
[50] V. Rodin, F. Symalla, V. Meded, P. Friederich, D. Danilov, A. Poschlad, G. Nelles, F. von Wrochem, W. Wenzel, *Phys. Rev. B* **2015**, *91*, 155203.